Dynamical spin susceptibility in La$_2$CuO$_4$ studied by resonant inelastic x-ray scattering

H. C. Robarts,[1,2] M. García-Fernández,[1] J. Li ®,[1,3] A. Nag ®,[1] A. C. Walters,[1] N. E. Headings,[2]
S. M. Hayden,[2,*] and Ke-Jin Zhou ®[1,†]

[1]*Diamond Light Source, Harwell Campus, Didcot OX11 0DE, United Kingdom*
[2]*H. H. Wills Physics Laboratory, University of Bristol, Bristol BS8 1TL, United Kingdom*
[3]*Beijing National Laboratory for Condensed Matter Physics and Institute of Physics, Chinese Academy of Sciences, Beijing 100190, China*

Resonant inelastic x-ray scattering (RIXS) is a powerful probe of elementary excitations in solids. It is now widely applied to study magnetic excitations. However, its complex cross section means that RIXS has been more difficult to interpret than inelastic neutron scattering (INS). Here we report ∼37 meV resolution RIXS measurements of the magnetic excitations in La$_2$CuO$_4$, the antiferromagnetic parent of one system of high-temperature superconductors. At high energies (∼2 eV), the RIXS spectra show angular-dependent dd orbital excitations in agreement with previous RIXS studies but show new structure. They are interpreted with single-site multiplet calculations. At low energies (≲0.3 eV), we model the wave-vector-dependent single magnon RIXS intensity as the product of the calculated single-ion spin-flip RIXS cross section and the dynamical structure factor $S(\mathbf{Q}, \omega)$ of the spin-wave excitations. When $S(\mathbf{Q}, \omega)$ is extracted from our data, the wave-vector-dependence of the single-magnon pole intensity shows a similar variation to that observed by INS. Our results confirm that suitably corrected RIXS data can yield the genuine wave-vector and energy dependence of $S(\mathbf{Q}, \omega)$ for a cuprate antiferromagnet. In addition to spin waves, our data show structured multimagnon excitations with dispersing peaks in the intensity at energies higher than the single-magnon excitations.

I. INTRODUCTION

Unconventional superconductors constitute an important group of strongly correlated materials that include heavy fermions, cuprates, ruthenates, and iron-based superconductors [1–4]. They show a proximity to magnetic ordering or have strong magnetic fluctuations [5]. In some cases, the superconductivity can be established by chemical doping or pressurizing a magnetic parent compound. Although the long-range magnetic order is suppressed by the external tuning, the short-range magnetic fluctuations are found to survive in the superconducting phase of many unconventional superconductors [6–12]. The importance of these magnetic fluctuations to the superconducting pairing mechanism has been a subject of many studies in the last decades [5,13].

Experimentally, inelastic neutron scattering (INS) is a well-established probe for the magnetic fluctuations in magnetic materials providing direct measurement of the magnetic structure factor $S(\mathbf{Q}, \omega)$ [14]. For example, in La$_2$CuO$_4$ (LCO), the parent compound of the first reported cuprate superconductors, INS measurements observed spin-wave excitations throughout the Brillouin zone [15,16]. The excitations are described by large superexchange couplings within the CuO$_2$ planes, which extend beyond nearest neighbors. INS has also shown that magnetic excitations persist over a large range of wave vectors in superconducting cuprates [11]. They are particularly strong near the (1/2, 1/2) position.

Compared to INS, RIXS is a newly emerged technique, which has been proven to be a powerful tool for probing magnetic excitations in transition-metal oxides [17,18]. Owing to its high cross section and micron-size focused x-ray beam, RIXS is advantageous over INS in measuring small samples and nanometer-thick films. By working at a resonance, RIXS is element specific thus particularly suited for probing magnetic fluctuations in complex systems with multiple magnetic elements. INS measurements of collective magnetic excitations become technically challenging above about 500 meV because the background due to multiple scattering becomes large. RIXS does not suffer from this problem thus has a major advantage for measuring high-energy excitations.

RIXS has made good contributions to the study of spin excitations in cuprates. One of the earliest high-resolution RIXS measurements at the Cu L edge in LCO demonstrated spin excitations have similar dispersion as INS [19]. Subsequent measurements on a wide range of cuprate superconductors have revealed rich information about the damping, the incident energy dependence, the x-rays polarization dependence, and the spectral weight of the spin fluctuations as a function of the doping level [12,20–28]. Most recently, the dispersions of RIXS magnetic excitations across a significant portion of the reciprocal space in various cuprate compounds were shown to

---

*s.hayden@bristol.ac.uk
†kejin.zhou@diamond.ac.uk

agree with the spin-wave theory [29]. Beyond cuprates, RIXS has also demonstrated to be capable of probing magnetic excitations in two-dimensional (2D) nickelates and iridates [30,31]. These works clearly establish RIXS as a quantitative probe of the dispersions of magnetic excitations in magnetic insulators.

Theoretically, the relationship between RIXS cross section and different correlation functions was investigated via a perturbative expansion of the RIXS operator, i.e., the ultrashort core-hole lifetime expansion (UCL) [18], or via the effective operator approach [32]. These studies confirm that the low-energy RIXS is governed by spin excitations at least in magnetic insulators. For the doped systems, the situation becomes much more complex as both spin and charge excitations may contribute to the low-energy regime of RIXS spectra. Still both the UCL and the nonperturbative effective operator approaches were used to explore RIXS spin excitations and some general understandings were obtained [33,34].

Despite vast amount of RIXS measurements on magnon dispersions, magnetic RIXS spectral weight has been explored much less due to its complex cross section and often relative comparisons are adopted [21,22,35]. Ament *et al.* [18] pointed out that under certain theoretical approximations, the absolute RIXS cross section is proportional to the atomic form factor multiplied by a dynamic structure factor $S(\mathbf{Q}, \omega)$. Such an approach has been applied to perovskite cuprates and nickelates in studying magnetic RIXS intensities [36,37]. Braicovich *et al.* [36] studied magnetic excitations in a number of undoped cuprates and found good agreement between measured and calculated the momentum and polarization dependence of single-magnon RIXS spectral weight. This was demonstrated by the linear dichroic ratio of the RIXS spectral weight between the horizontal and vertical polarizations assuming that the dynamical structure factor $S(\mathbf{Q}, \omega)$ could be divided out as a technique independent component. In a very recent study of doped La$_{2-x}$Sr$_x$CuO$_4$ (LSCO), a similar procedure was applied to determine the absolute wave-vector-dependent susceptibility [38]. In this work, the atomic form factor is regarded the same between the parent LCO and the doped LSCO compounds. Magnetic RIXS spectral weights were then compared using the absolute unit by assuming the dynamical structure factor $S(\mathbf{Q}, \omega)$ in LCO measured by RIXS to be equivalent to those obtained from INS data.

Here we aim to improve the understanding of the magnetic RIXS cross section by examining the validity of the assumption made for LCO in the previous study [38], that is, whether indeed the dynamical structure factor $S(\mathbf{Q}, \omega)$ probed by RIXS is consistent to the spin-wave theory and INS results. RIXS measurements were performed on LCO single crystals with surface normals (001) and (100). The sample with the surface normal (100) provides extra access along the (h, h) direction in reciprocal space compared to previous RIXS measurements. We first compare the measured and calculated dd orbital excitations using ligand-field theory (LFT) implemented in the many-body code QUANTY [39,40]. Good agreement was obtained for both samples. The comparison was then extended to the magnetic excitations. Instead of normalizing the RIXS intensity of the magnetic scattering to the measured dd excitations [36], we studied in detail the atomic form factor for the single-ion spin-flip RIXS excitations.

The extracted wave-vector-dependent spin susceptibilities $\chi'(\mathbf{Q})$ show a remarkable match with those seen by INS.

II. RIXS EXPERIMENTS

The RIXS experiments were performed on single-crystal samples of LCO, which were grown using the traveling solvent floating zone technique. We describe LCO using its high-temperature tetragonal (HTT) I4/mmm crystal structure in which $a = b \simeq 3.8$ Å, $c \simeq 13.2$ Å. The momentum transfer $\mathbf{Q}$ is defined in reciprocal lattice units (r.l.u.) as $\mathbf{Q} = h\mathbf{a}^* + k\mathbf{b}^* + l\mathbf{c}^*$ where $\mathbf{a}^* = 2\pi/a$, etc. The energy of the scattered photons is given by $\hbar\omega = c|\mathbf{k}| - c|\mathbf{k}'|$ and momenta $\mathbf{Q} = \mathbf{k} - \mathbf{k}'$, where $\mathbf{k}$ and $\mathbf{k}'$ is the incident and scattered photon wave vector, respectively.

High-resolution RIXS spectra were acquired at the I21-RIXS Beamline at Diamond Light Source, United Kingdom [41]. The incoming x-ray photon energy was tuned to the Cu L_3 resonance ($\simeq$931.5 eV) and we performed measurements with both linear horizontal (LH)/π polarization and linear vertical (LV)/σ polarization (Fig. 1). The total instrumental energy resolution has standard Gaussian distribution with the
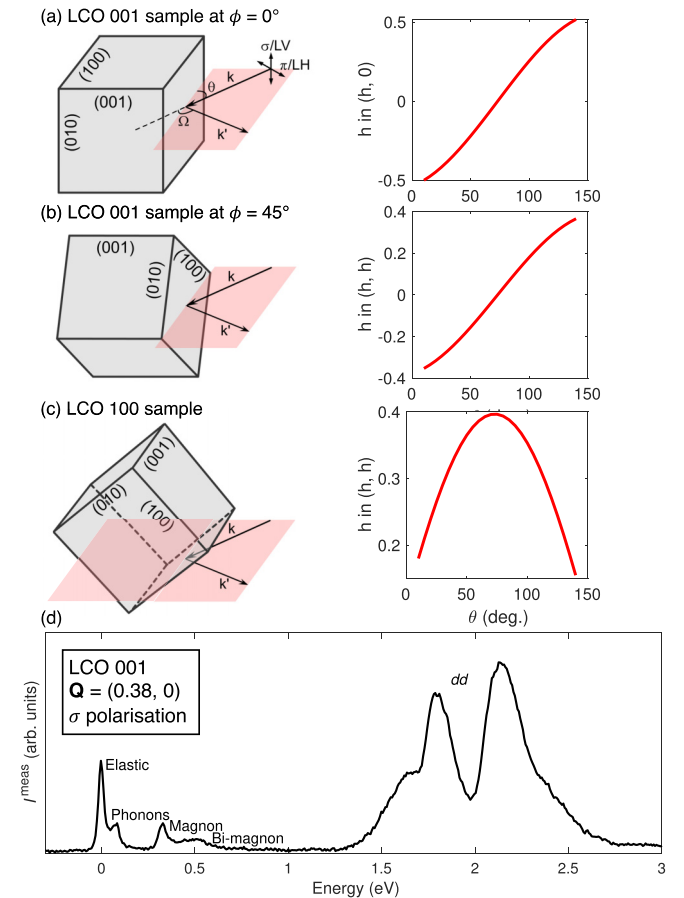

FIG. 1. RIXS experimental geometries for the two samples. (a) The LCO001 sample at $\phi = 0^\circ$, probing $(h, 0)$. (b) The LCO001 sample at $\phi = 45^\circ$, probing (h, h). (c) The LCO100 sample probing (h, h). For each orientation, the projection of the momentum transfer and the relationship between θ and the momentum transfer is shown. (d) shows various excitations resolved in a typical RIXS spectrum.

full width at the half-maximum of $\Delta E \simeq 37$ meV. All RIXS measurements were conducted at 15 K without the outgoing polarization analysis.

Two different samples, LCO001 and LCO100, were prepared with the surface normals (001) and (100), respectively. The samples were aligned and cleaved *in situ* to expose a clean surface to the beam. Figures 1(a) and 1(b) shows how data were collected from LCO001 along $(h, 0)$ and (h, h), respectively. Figure 1(c) shows how LCO100 was mounted on a 45° wedge such that $(1\bar{1}0)$ was perpendicular to the scattering plane. This allowed data to be collected along (h, h) to larger h. Because of the two-dimensionality of the magnetic excitations in cuprates, the in-plane wave vector (h, k) is varied by scanning the angle of incidence θ while keeping the scattering angle, Ω, fixed at 154°. The zero of θ ($\theta = 0$) is defined such that (110) is antiparallel to **k** and "grazing-in" **k** probes negative h. Thus with LCO001, we access $(h, 0) = (-0.5, 0)$ to $(0.5, 0)$ and $(h, h) = (-0.35, -0.35)$ to $(0.35, 0.35)$. For LCO100, (h, h) is probed with a maximal in-plane wave vector of $(0.4, 0.4)$.

A typical RIXS spectrum is shown in Fig. 1(c) in which a quasielastic peak, phonon excitations, single-magnon, multimagnon, and dd orbital excitations are clearly resolved. The measured RIXS intensity, $I_{\sigma(\pi)}^{\text{meas}}$ can be corrected to yield the real RIXS intensity $I_{\sigma(\pi)}^{\text{corr}}$, to account for energy, wave-vector, and polarization-dependent self-absorption effects. The self-absorption correction method is an extension of the simple procedure in recent works [26,42] and is described explicitly in Appendix A 3. In Sec. III, we will first focus on the dd orbital excitations and in Sec. IV, we will discuss the magnetic excitations.

III. dd ORBITAL EXCITATIONS

The RIXS spectra are dominated by strong dd excitations between 1.3 and 3 eV, which occur due to transitions between the ground and the excited $3d$ orbital states as sketched in Fig. 2(a). dd excitations have been extensively studied using RIXS in the past for understanding the local crystal field splittings among various cuprate families [43,44]. Plotted in Fig. 2(b) is a representative RIXS spectrum in the energy range of the dd excitations. More experimental RIXS dd spectra are presented in Fig. 10 in Appendix A. Overall they are consistent to a previous report besides the d_{z^2} orbital is better resolved [44]. A pseudo-Voigt function is used for the spectral fitting where each dd excitation seems to comprise two peaks in particular the d_{xy} orbital. The averaged splitting energy is about 100 meV. The double-peak profile in each orbital excitation is possibly due to the coupling with the spin-flip or phonon excitations [45,46]. There is also additional spectral weight present at a higher energy of 2.4 eV. This peak is seen in a previous work and has been attributed to oxygen vacancies, which are thought to alter the crystal field acting on the Cu ions [44]. We fit this peak with an additional pseudo-Voigt function.

To reproduce the experimental observations, we constructed a single $(CuO_4)^{6-}$ cluster in D_{4h} symmetry using ligand-field multiplet theory (LFT) implemented in the many-body QUANTY code [39,40]. To simplify the multi-
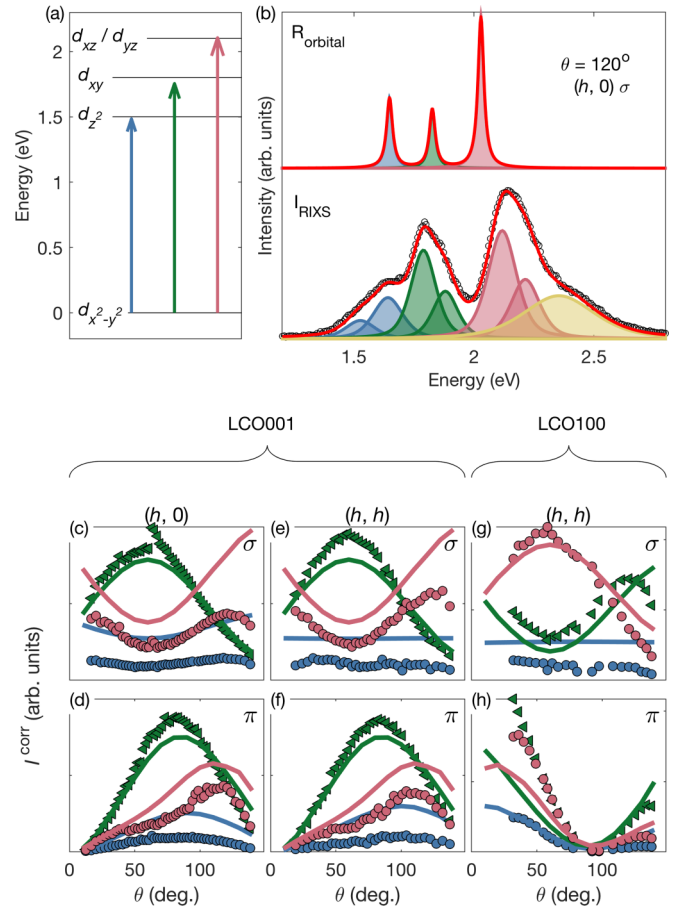

FIG. 2. Orbital excitations in RIXS showing (a) the dd transitions in LCO and (b) a comparison of the calculated dd peaks from ligand field theory (LFT) and RIXS measurements for a typical spectrum at $\theta = 120°$ along the $(h, 0)$ direction, LCO001 orientation and with σ polarization. (c)–(h) show the intensity of the dd excitations from fitted RIXS data compared with the relative intensities calculated in LFT.

plet calculations, we consider pure dd orbital excitations without invoking the spin-flip or phonon contributions in dd. Throughout the paper, all calculations were done with the outgoing polarization effect averaged and spectra are broadened with the instrumental energy resolution. Appendix B describes the calculation details. As the dd excitations are dispersionless (without **Q** dependence) [17], the self-absorption corrected orbital excitations intensity can be described by the atomic form factor, i.e., the single-ion orbital excitation amplitude, $R_{\text{orbital}}(\boldsymbol{\epsilon}, \boldsymbol{\epsilon}', \omega)$, which is dependent on the polarization $\boldsymbol{\epsilon}$ and $\boldsymbol{\epsilon}'$ of the initial and final photons, and the excitation energy ω:

$$I_{\text{orbital}} = f'_{\text{orbital}} \times R_{\text{orbital}}(\boldsymbol{\epsilon}, \boldsymbol{\epsilon}', \omega). \quad (1)$$

f'_{orbital} is a constant prefactor for the orbital excitation intensity. Figure 2(b) compares the theoretical calculated result to the RIXS measurements for a representative spectrum. It is noticeable that the experimental excitations are much broader than that in the LFT theory. In addition, the relative intensity of d_{z^2} orbital is overestimated in theory. To further explore the

comparison, we extended the study to the angular dependence of the *dd* orbital excitations.

In Figs. 2(c)–2(h) we summarize the integrated *dd* orbital excitation intensity as a function of θ under various experimental configurations. Note that each data point represents the sum of the full integrated area of each *dd* orbital excitation. The angular-dependent theoretical results are superimposed on top of the experimental data. Note that the calculated *dd* excitation intensities have been renormalized using a single scaling factor for all orbital excitations in order to compare with the experimental data. We notice that LFT theory describes well d_{xy} and d_{xz}/d_{yz} orbitals though overestimates at close to the grazing-out geometry, $\theta > 100^{\circ}$, with σ polarization along both $(h, 0)$ and (h, h) directions. For d_{z^2} orbital, LFT seems to overestimate generally for most of the experimental configurations indicating potentially the insufficiency of a single $(CuO_4)^{6-}$ cluster. Nevertheless, the overall θ dependence of *dd* excitations seems to match with the theory for all experimental configurations. We are therefore motivated to apply the theory to the magnetic excitations whose intensities are strongly θ dependent [17].

IV. DYNAMICAL SPIN SUSCEPTIBILITY

Figures 3(a)–3(f) show RIXS intensity maps in the low-energy region as a function of the momentum transfer along (100) and (110) directions. Near zero energy loss, we see quasielastic peaks. Between zero and 100 meV, two phonon branches are clearly resolved throughout the accessible momentum space. These are likely the bond-buckling and the bond-stretching modes [47], which will be discussed in a separate work. As is known, the strongly dispersive features are single magnons emanating from the zone center to the zone boundary up to almost 400 meV [15,16]. In particular, single magnons in LCO100 show consistent dispersion compared to that in LCO001 projected along the (h, h) direction. Beyond the zone boundary of $(1/4, 1/4)$, the single magnons continue to disperse to lower energy akin to the INS data [Figs. 3(c)–3(f)] [15,16]. Broader peaks appear between 400 meV and 600 meV, which are most likely the multimagnons as observed by RIXS at the Cu L_3 and the O K edges [48,49].

The spectra between −80 and 800 meV are modeled with Gaussian functions to account for the elastic peak and phonons and with the response function of a damped harmonic oscillator (DHO) to account for the (single- and multi)magnon excitations. The DHO model has been used in several RIXS studies [38,50,51] and describes the response for a range of damping. We fit the spectra to the imaginary part of the DHO response, given by,

$$\chi''(\mathbf{Q}, \omega) = \frac{\chi'(\mathbf{Q})\,\omega_0^2(\mathbf{Q})\,\gamma(\mathbf{Q})\,\omega}{\left[\omega^2 - \omega_0^2(\mathbf{Q})\right]^2 + \omega^2\gamma^2(\mathbf{Q})}, \tag{2}$$

where $\chi'(\mathbf{Q})$ is the real part of the susceptibility at zero frequency, ω_0 describes the position of the excitation pole and γ represents the damping.
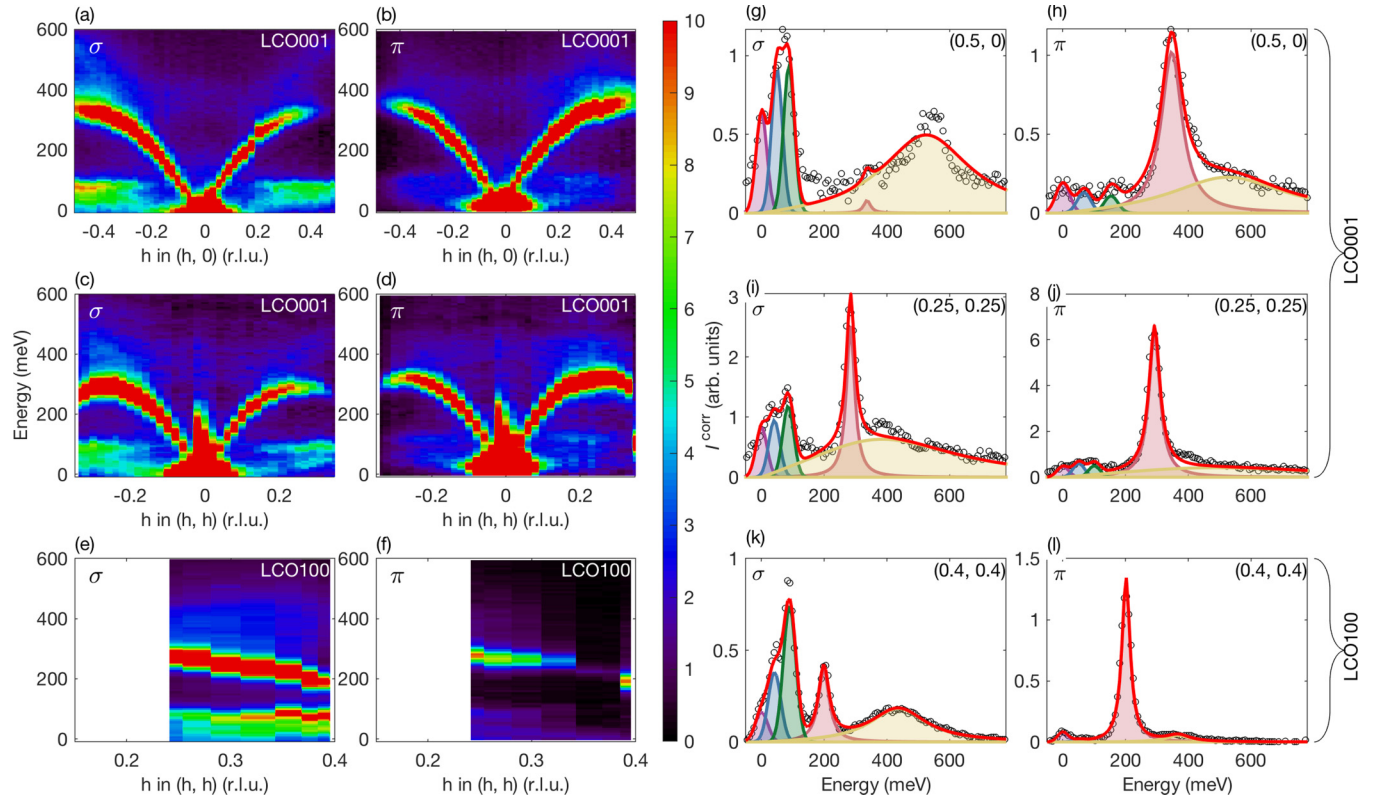

FIG. 3. The low-energy excitations in LCO showing (a)–(f) self-absorption corrected RIXS intensity maps and (g)–(l) representative RIXS spectra. Total fits to the data are shown in red. The DHO magnon and multimagnon fit are shown in pink and yellow, respectively. Gaussian fits to the elastic peak (purple) and phonon (blue and green) peaks.

Examples of the RIXS spectra and fittings are shown in
Figs. 3(g)–3(l). The data show drastically different ratio be-
tween the single- and multimagnon intensity measured with
incident polarization σ or π. At $\mathbf{Q} = (1/2, 0)$, the single-
magnon component dominates the spectra for π polarization
while it becomes much weaker and almost entirely obscured
by the multimagnon component with σ polarization. The
drastic polarization and θ dependence is due to the local
spin-flip cross section [17]. Interestingly, the multimagnon
at $\mathbf{Q} = (1/2, 0)$ probed with σ polarization in Fig. 3(g) has
a well-defined line profile and cannot be fitted by DHO.
It is also the enigmatic region $(1/2, 0)$ where INS reported
the spin excitations deviate from the linear spin-wave theory
[16]. Very recently a polarimetric RIXS study revealed well-
structured multimagnon excitations in the parent $Sr_2CuO_2Cl_2$
at the same zone boundary position [52]. The polarimetric
RIXS analysis shows that the mode cannot reconcile with
pure bimagnon excitations and higher-order magnons, such
as three-magnon excitations, likely contribute to the spectral
weight at the specific region [53].

To illustrate the single-magnon dispersion more clearly, we
plot the magnetic pole ω_0 of LCO001 in Figs. 4(a)–4(d). On
top of that, we add data points obtained from LCO100 along
the (h, h) direction. Noticeably, the single-magnon disper-
sion obtained from LCO001 and LCO100 matches very well.
To compare with the spin-wave theory (SWT), we computed
the dispersion using the nearest- and the next-nearest-
neighbor exchange constants extracted from INS [16]. Good
agreement is seen in both $(h, 0)$ and (h, h) direction. Fig-
ures 4(e) and 4(f) show comparisons of the magnon spectra
obtained between RIXS and INS at two zone boundary po-
sitions. Remarkably, the line shape of the magnon spectra
agree well between two techniques. At the $(1/4, 1/4)$, the
magnon excitation shows a resolution-limited peak whereas
at $(1/2, 0)$, both RIXS and INS spectra present some spectral
weight at high energy as a continuum.

We now discuss the RIXS intensity of the single magnons.
As with the analysis of the dd excitations, the single-magnon
intensities are extracted from an integration of the DHO func-
tion and summarized in Figs. 5(a)–5(f). Note that these data
are presented as a function of θ due to the complex projection
along the (h, h) direction in LCO100. Importantly, as the sin-
gle magnons are strongly dispersive in the energy-momentum
space, an accurate self-absorption correction is performed for
both the energy and momentum dependence. Details of the
self-absorption correction are presented in Appendix A 3. At
least for the magnetic insulators [17], RIXS magnon intensity
is proportional to the dynamical structure factor $S(\mathbf{Q}, \omega)$ mul-
tiplied by the atomic form factor of the single-ion spin-flip
amplitude, $R_{spin}(\epsilon, \epsilon', \omega)$, which is dependent on the polariza-
tion ϵ and ϵ' of the initial and final photons, and the excitation
energy ω:

$$I_{spin} = f'_{spin} \times R_{spin}(\epsilon, \epsilon', \omega) \times S(\mathbf{Q}, \omega). \tag{3}$$

f'_{spin} is a constant prefactor for the spin excitation intensity.
Under this approximation, we computed the single-ion spin-
flip amplitude, R_{spin}, as a function of θ. To simulate the
single-ion spin-flip excitation, we add a magnetic field along
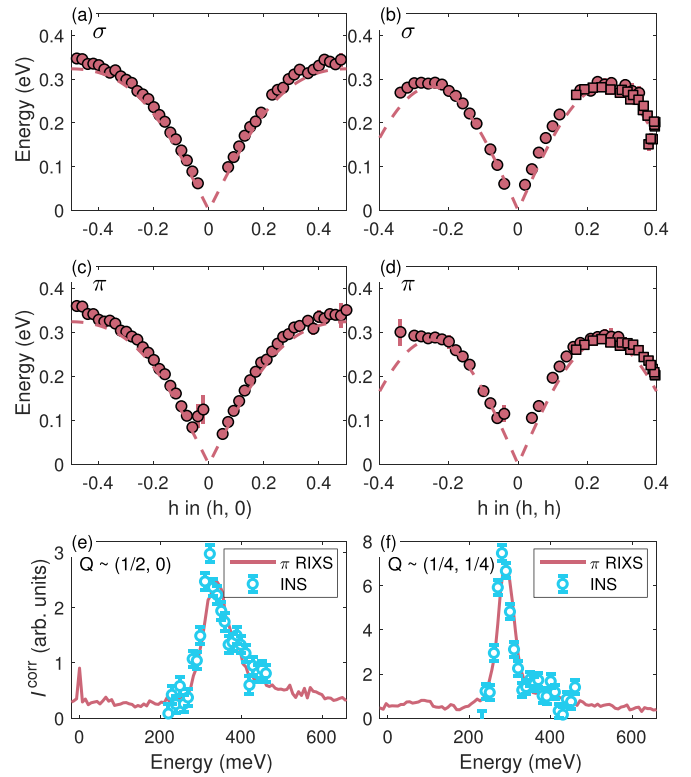the (h, h) direction of the CuO_2 planes with a magnitude

FIG. 4. (a)–(d) show the energy dispersion of magnon excitations
measured by RIXS. Red symbols indicate ω_0 extracted from the
damped harmonic oscillator fit to the magnons and data from the
LCO001 and LCO100 orientations are indicated with circles and
squares, respectively. The dashed line shows the magnon dispersion
extracted from INS [16]. (e)–(f) show comparison of the magnon
line shape measured with π polarized RIXS in pink and INS in cyan,
at wave vectors close to $(1/2, 0)$ and $(1/4, 1/4)$. The INS data are
scaled to the RIXS data and a constant offset of 0.5 is added to the
INS to compensate for a possible over subtraction of the background
in Ref. [16].

resulting in Zeeman splittings in the order of 100 meV. The
calculated spin-flip spectra were fitted using DHO function
and the integrated spectral weight are plotted on top of the
experimental data in Figs. 5(a)–5(f).

The first glimpse informs us that the experimental magnon
intensities modulate as a function of θ and follow the overall
trend of the local spin-flip cross section at least for LCO001.
However, there are deviations around $\theta \simeq 75°$ where the
magnon intensity drops almost to zero. This is probably due
to the diminished spin-wave intensity near the zone center.
It is thus appealing to see both the local and the collective
behaviors play a role in the magnon intensities in RIXS.
For LCO100, it is less obvious to trace the evolution of the
magnon intensities between the experiment data and the local
spin-flip cross section. This may be due to the unusual projec-
tion of the momentum transfer along the (h, h) direction.

To reveal the dynamic spin susceptibility from RIXS, we
divided the magnon intensity by the local RIXS spin cross
section from the LFT calculations,

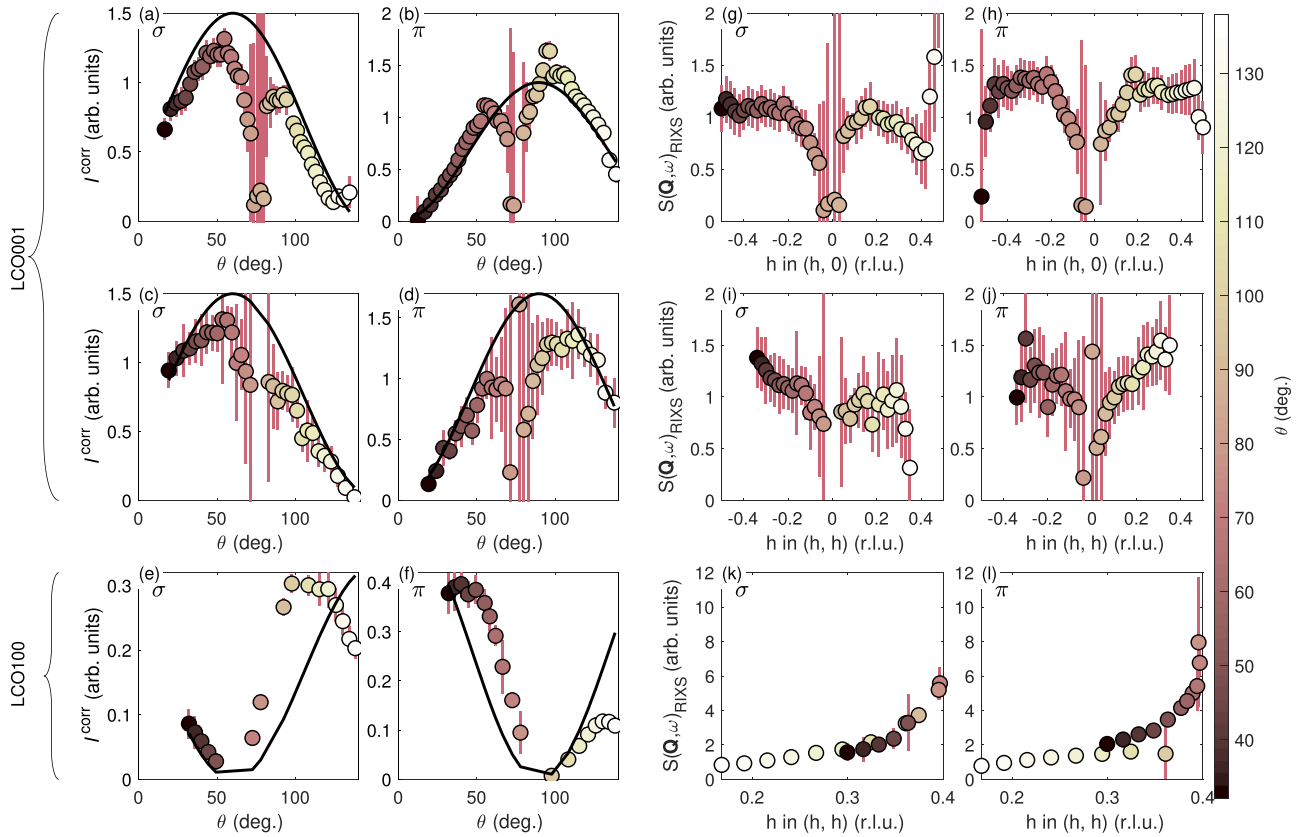$$S(\mathbf{Q}, \omega)_{RIXS} \propto \frac{I_{spin}}{R_{spin}}. \tag{4}$$

FIG. 5. Details of the deconvolution procedure for the magnon intensity. (a)–(f) show the self-absorption corrected magnon intensity, I_{corr} (filled circles), compared to the single-ion spin-flip cross section R_{spin} (black line). (g)–(l) show the fully deconvoluted intensity, $S(\mathbf{Q}, \omega)_{RIXS}$ as a function of $\mathbf{Q}$. The value of θ is indicated by the color.

$S(\mathbf{Q}, \omega)_{RIXS}$ is shown for both LCO001 and LCO100 in Figs. 5(g)–5(l) as a function of wave vector. Remarkably, the simple process yields a highly symmetrical intensity profile with respect to the zone center in LCO001 along both $(h, 0)$ and (h, h) directions. The symmetrical magnon intensity profile is reminiscent of the spin-wave intensity in the Heisenberg model [15,16]. For LCO100, the difference after the removal of the local spin-flip cross section is even more striking. The irregular magnon intensity profile evolved to a clear exponential-like trend as a function of $\mathbf{Q}$ along the (h, h) direction consistent to the linear spin-wave theory and the INS data [15,16]. We want to bring the attention to the effect of the incident x-ray polarizations. The fact that there is almost no polarization dependence among all sets of data pointing to a simple message, that is, the pure collective dynamic spin susceptibility is independent of the property of the experimental probe. It is also worth mentioning the error bars of the magnon intensities. For LCO001, data points near the zone center are marked with large error bars due to the uncertainty of fitting the negligible raw magnon intensities. Similarly, the data points near the very grazing-out (grazing-in) geometry in σ (π) polarization are associated with large error bars as a result of minimal local spin-flip cross section. The latter reason also applies to LCO100 where the large error bars are present near $\theta \simeq 60°$ and $90°$ for σ and π polarizations, respectively.

Figure 6 shows the single-magnon intensity measured with INS by Headings *et al.* along the primary direction $(h, 0)$ and
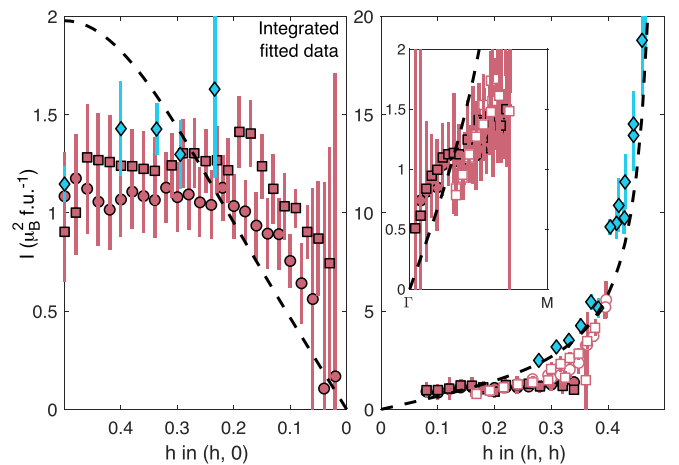

FIG. 6. Comparison of the spin-wave intensity for RIXS, INS, and the theoretical values from SWT. INS data are shown as blue diamonds and the SWT as a black dashed line. RIXS data from the LCO001 and LCO100 orientation are indicated in pink and white marks, respectively, and σ and π polarization are represented by circles and squares, respectively. In each case I is the energy integral of $S(\mathbf{Q}, \omega)$ over the spin-wave pole.

(h, h), as well as the linear spin-wave intensity calculated from the next-next-nearest-neighbor SWT model [16]. Along the $(h, 0)$ direction, INS data show roughly a constant magnon intensity profile from 0.2–0.5 r.l.u.. Such behavior is a clear deviation from the linear spin-wave theory, which increases monotonically approaching the zone boundary. The missing spectral weight was explained due to the cutoff energy of 450 meV in INS and the creation of a spinon pair at $(1/2, 0)$ [16]. To verify this, we plot $S(\mathbf{Q}, \omega)_{RIXS}$ results in Fig. 6. Note that RIXS data are selected from regions with relative small error bars, i.e., σ grazing-in, π grazing-out for LCO001, while σ grazing-out and π grazing-in for LCO100. In particular, a single scaling constant is applied to the RIXS data in order to compare the relative trend of $S(\mathbf{Q}, \omega)_{RIXS}$ with respect to INS results. It is interesting to find that RIXS measurements up to 1 eV yield similar results. The comparison highlights that the discrepancy at the zone boundary of $(1/2, 0)$ between the experimental results and the SWT has physical origin and is not influenced by the technical limitation of the energy cutoff in INS.

Along the (h, h) direction, LCO100 shows a sharp intensity increase towards the $\mathbf{Q}_{AFM} = (1/2, 1/2)$. We see vague indication of the trend in LCO001, however, the measurements do not reach large enough $\mathbf{Q}$. The measurements on LCO100 allows us to reach $(0.4, 0.4)$, which is crucial for the comparison with INS experimental data. The level of agreement is good among RIXS, INS, and SWT model, which all show an increased intensity toward the $\mathbf{Q}_{AFM} = (1/2, 1/2)$. At low $\mathbf{Q}$, RIXS generally observes greater spectral weight than INS. The additional intensity may well result from the specular reflection influencing the magnon fits.

The intensity of the multimagnon excitations, which are well resolved in our data, could be extracted and corrected in the same way as the single magnons. However, the polarization dependence and the line shape of the multimagnon excitations are not fully understood [52]. The single-site calculations are also inadequate in this case as multimagnon creation is likely to be more complex [17,53] than simple bimagnon excitations. Cluster calculations are needed to provide a proper description of the multiple-sites spin-flip cross section before the extraction of the dynamical spin susceptibility of the multimagnons.

V. CONCLUSIONS

We have made high-resolution RIXS measurements of the orbital and collective magnetic excitation for La_2CuO_4 single crystals with the surface normals (001) and (100). The dd orbital excitations are clearly resolved owing to the high-energy resolution. Strong θ dependence of the orbital excitations are well reproduced by the multiplet ligand field theory. The momentum-dependent collective magnetic excitations are measured along both $(h, 0)$ and (h, h) directions of the first Brillouin zone to the extent that is possible at the Cu L_3 edge. The dispersion of the single magnons show a very good match to the spin-wave theory. Remarkably, the RIXS single-magnon spectral profiles are reminiscent of those measured by INS. We determined the wave-vector-dependent single-magnon response by correcting for the self-absorption and the atomic form factor of the local spin-flip amplitude. It

is found that this response reflects the well-known dynamical spin susceptibility for La_2CuO_4 regardless of the incident photon polarization and the many-body effects involved in the RIXS process. Comparing to INS data, RIXS show excellent agreement along both primary directions. In particular, the consistent results between RIXS and INS show strong deviation from the spin-wave theory indicating the abnormal spin susceptibility approaching $(h, 0)$ zone boundary is a genuine behavior of the system.

APPENDIX A: EXPERIMENTAL DETAILS

1. Sample preparation

Samples of single-crystal LCO were grown via the traveling-solvent floating zone technique (TSFZ), annealed in an argon atmosphere to remove excess oxygen, detwinned and cleaved *in situ*. The crystals were previously used in the neutron scattering measurements described in Ref. [16].

2. Data processing

RIXS data are extracted by integrating along the non-energy-dispersive direction at each $\mathbf{Q}$ after subtracting the dark-image background. Spectra are normalized by the counting time. The zero-energy positions of RIXS spectra were determined by comparing to reference spectra recorded from the amorphous carbon tapes next to the sample for each $\mathbf{Q}$ position. They were finely adjusted through the Gaussian fitting of each elastic peak. It is clear that this process is much easier close to the specular position ($\mathbf{Q} = 0$ in the LCO001 orientation) where the elastic peak becomes large. To reflect this, the error in the energy correction is established by the error in fitting a Gaussian peak multiplied by a Bose function $n(\omega) + 1$ to model the excitations near $\omega = 0$. The shift in energy remains within 12 meV throughout the $\mathbf{Q}$ range, therefore we conclude that the procedure is consistent regardless of the intensity of the elastic peak.

3. Self-absorption correction

We follow recent practice [26,28,54–56] to correct for the effects of self-absorption in our data using x-ray absorption spectra (XAS) measured in the same geometry as the RIXS measurements. We estimate a self-absorption factor, C_{SA} using the same procedure as outlined in Ref. [38], where the
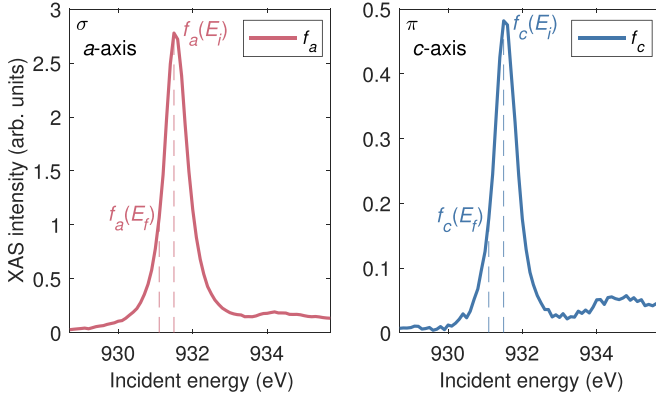
FIG. 7. The projected XAS spectra along the a and c axes in LCO samples with σ and π polarizations. $f_a(E_i)$, $f_c(E_i)$ have fixed intensity due to the fixed incident energy while $f_a(E_f)$, $f_c(E_f)$ of emitted x rays are energy dependent.

corrected intensity $I^{corr}_{\sigma(\pi)}$ is $I^{corr}_{\sigma(\pi)} = C_{SA} I^{meas}_{\sigma(\pi)}$ or,

$$I^{corr}_{\sigma(\pi)} = I^{meas}_{\sigma(\pi)} \frac{\mu_{i,\sigma(\pi)} \sin(\Omega - \theta) + \mu_{f,\sigma(\pi)} \sin\theta}{\sin(\Omega - \theta)}. \quad \text{(A1)}$$

Here μ_i and μ_f are the absorption coefficients extracted from XAS performed prior to the RIXS measurements. In our experiments the XAS is measured with the total electron yield. Components of the photon form factor, f_a and f_c, are extracted from the XAS intensity when the electric field of the incident x rays is parallel to the crystalline a and c axes, respectively which can be accessed with σ and π polarized x rays, respectively. Figure 7 shows example XAS spectra measured along

the a and c axes. f_a and f_c are found from the intensity of the XAS spectra at E_i and E_f relative to the intensity at resonance. These values allow us to estimate the absorption coefficients for the incident and outgoing x rays in the LCO001 geometry,

$$\mu_{i,\sigma} = f_a(E_i),$$
$$\mu_{i,\pi} = f_a(E_i) \sin^2\theta + f_c(E_i) \cos^2\theta,$$
$$\mu_{f,\sigma} = f_a(E_f),$$
$$\mu_{f,\pi} = f_a(E_f) \sin^2(\Omega - \theta) + f_c(E_f) \cos^2(\Omega - \theta). \quad \text{(A2)}$$

For LCO100 the absorption coefficients can be approximated as,

$$\mu_{i,\sigma} = f_a(E_i),$$
$$\mu_{i,\pi} = f_c(E_i) \sin^2\theta + f_a(E_i) \cos^2\theta,$$
$$\mu_{f,\sigma} = f_a(E_f),$$
$$\mu_{f,\pi} = f_c(E_f) \sin^2(\Omega - \theta) + f_a(E_f) \cos^2(\Omega - \theta). \quad \text{(A3)}$$

Taking these factors into account, Fig. 8 shows the energy, angle, and polarization dependence of the self-absorption factor, C_{SA}. A peak in self-absorption is seen close to the elastic position, which is most pronounced at large θ. However, it is clear that there is significant variation in the extent of self-absorption depending on the experimental setup.

Figure 9 shows the result of applying the self-absorption correction to the different excitations that were measured. Figures 9(a)–9(f) show the dd excitations intensity before and after the self-absorption correction. As shown in Fig. 8,
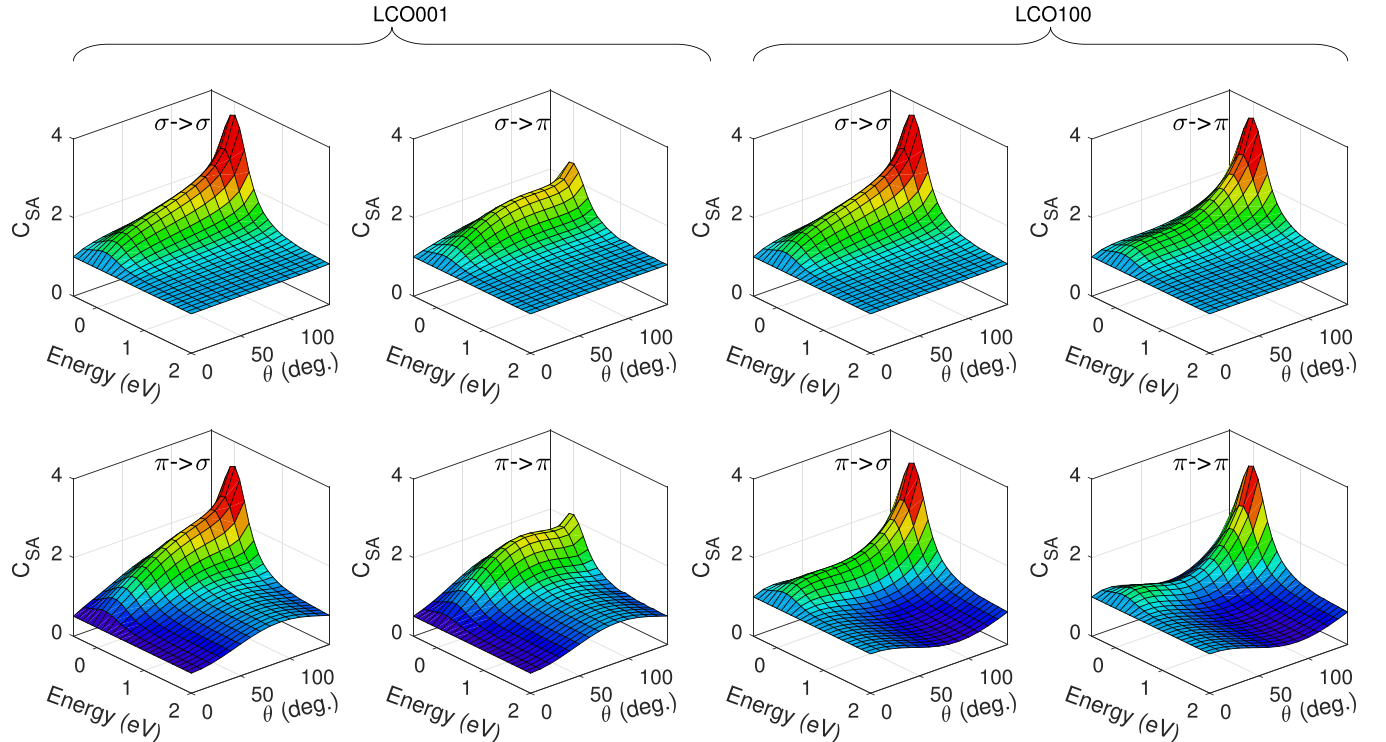

FIG. 8. The calculated self-absorption factor, C_{SA} for excitations measured in LCO as a function of excitation energy relative to Cu L_3 edge, incident angle θ and polarization.
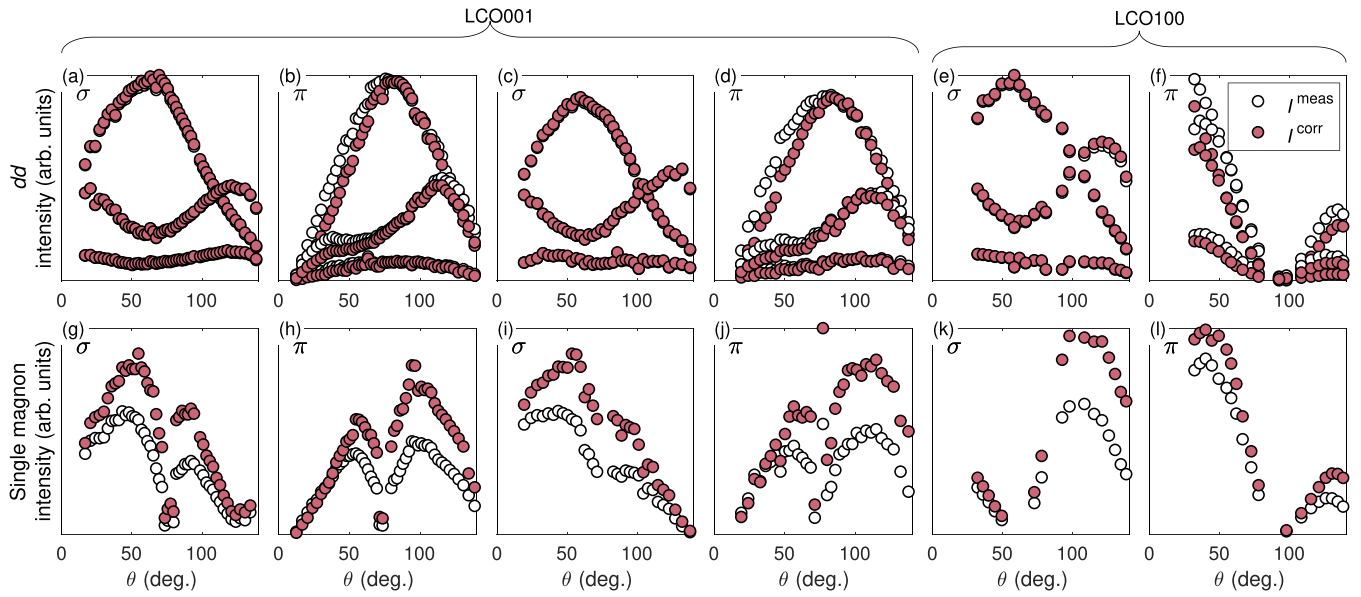
FIG. 9. RIXS intensity before and after applying the self-absorption correction. Measured data are shown in white and corrected data in red. The effect is shown for dd excitations in (a)–(f) and in single magnons in (g)–(l).

at the energy where the dd excitations occur, $\simeq 2$ eV, the self-absorption factor is relatively low, therefore the corrected intensity is not significantly changed. For dd excitations, we assume that the polarization of the scattered photons is unchanged ($\sigma \to \sigma$ or $\pi \to \pi$). This is an approximation that does not account for the complexity of the dd excitations

reported in Ref. [28] but as the total self-absorption at this energy is so small, this approximation works well enough for our purposes. Figure 10 presents raw dd excitation spectra under various configurations.

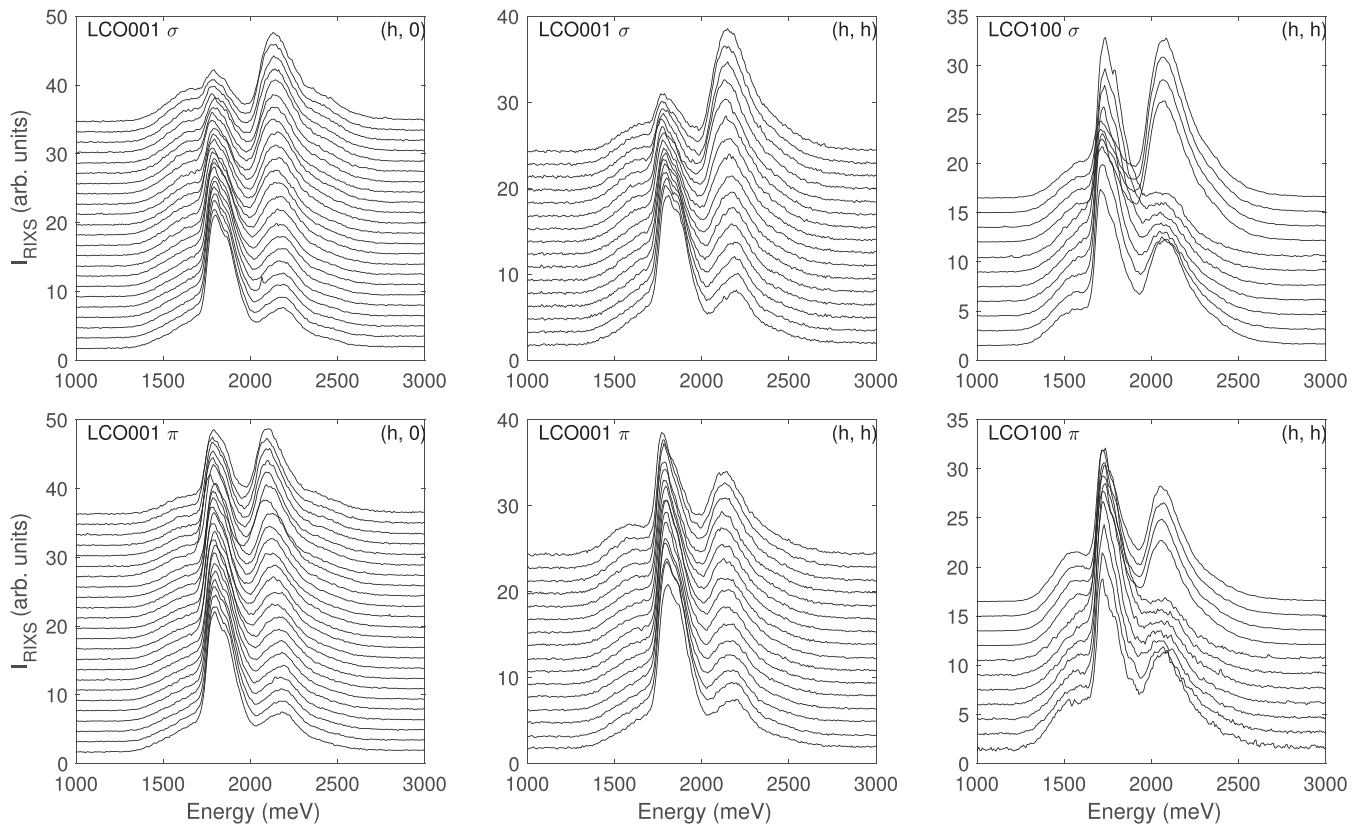At low energy, the self-absorption is much greater and polarization-dependence of the scattered light also becomes

FIG. 10. Experimental RIXS dd spectra under all configurations.

more significant. Figures 9(g)–9(l) show the intensity of the single-magnon excitations before and after the self-absorption correction. Here we assume the photon polarization is flipped as a result of the excitation ($\sigma \rightarrow \pi$ or $\pi \rightarrow \sigma$). This assumption is justified by RIXS measurements performed with polarization analysis such as that by Peng *et al.* [51] and Fumagalli *et al.* [28]. Following this assumption, the single-magnon intensity is seen to be significantly altered by the self-absorption effects.

APPENDIX B: LIGAND FIELD THEORY MULTIPLET CALCULATIONS

We computed the single-ion dd orbital and spin-flip excitations using ligand field theory implemented in the QUANTY package [39,40]. We implement the $(CuO_4)^{6-}$ cluster in D_{4h} symmetry in the LFT calculations [57]. The $3d$ states are therefore split into $d_{x^2-y^2}$, d_{z^2}, d_{xy}, and d_{xz}/d_{yz} orbitals under the D_{4h} symmetry. The ligand hole wave functions con-

sist of linear combination of O $2p$ orbitals with the above symmetries. The on-site d-hole energy is set to zero by omitting the point-charge crystal-field splitting. The energy of all unhybridized O $2p$ states is the charge-transfer energy Δ_{pd}. Owing to the nearest-neighbor O $2p$-O $2p$ hybridization, the effective charge-transfer energy of, the ligand hole with $d_{x^2-y^2}$ orbital symmetry, is $\Delta_{pd} - T_{pp}$, where T_{pp} is O $2p$-O $2p$ hopping integrals. Also, T_{pd} defines the Cu $3d$-O $2p$ hybridization energy for the $d_{x^2-y^2}$ orbital. We calculate the one-hole basis function, the matrix element and the energy levels as implemented in the Ref. [57]. To describe our RIXS data, we found the values of Δ_{pd}, T_{pp}, and T_{pd} are best optimized to 2.2 eV, 0.81 eV, and 3.1 eV, respectively, consistent to the previous study [44]. The values of the $3d$-$3d$ electrons Coulomb interaction Slater integrals, F_{dd}^0, F_{dd}^2, F_{dd}^4, F_{pd}^0, and F_{pd}^2, the $2p$ and $3d$ core-valence electrons exchange-Coulomb interaction Slater integrals G_{pd}^1 and G_{pd}^3, and the spin-orbit coupling of the ground state and the core-hole state, ξ_d and ξ_{2p}, are taken from Ref. [58].

[1] G. R. Stewart, Rev. Mod. Phys. **56**, 755 (1984).

[2] J. G. Bednorz and K. A. Müller, Z. Phys. B **64**, 189 (1986).

[3] Y. Maeno, H. Hashimoto, K. Yoshida, S. Nishizaki, T. Fujita, J. G. Bednorz, and F. Lichtenberg, Nature (London) **372**, 532 (1994).

[4] Y. Kamihara, H. Hiramatsu, M. Hirano, R. Kawamura, H. Yanagi, T. Kamiya, and H. Hosono, J. Am. Chem. Soc. **128**, 10012 (2006).

[5] D. J. Scalapino, Rev. Mod. Phys. **84**, 1383 (2012).

[6] K. B. Lyons, P. A. Fleury, L. F. Schneemeyer, and J. V. Waszczak, Phys. Rev. Lett. **60**, 732 (1988).

[7] S. M. Hayden, G. Aeppli, H. A. Mook, T. G. Perring, T. E. Mason, S.-W. Cheong, and Z. Fisk, Phys. Rev. Lett. **76**, 1344 (1996).

[8] P. Dai, H. A. Mook, R. D. Hunt, and F. Doğan, Phys. Rev. B **63**, 054525 (2001).

[9] C. Stock, W. J. L. Buyers, R. A. Cowley, P. S. Clegg, R. Coldea, C. D. Frost, R. Liang, D. Peets, D. Bonn, W. N. Hardy, and R. J. Birgeneau, Phys. Rev. B **71**, 024522 (2005).

[10] O. J. Lipscombe, S. M. Hayden, B. Vignolle, D. F. McMorrow, and T. G. Perring, Phys. Rev. Lett. **99**, 067002 (2007).

[11] N. S. Headings, S. M. Hayden, J. Kulda, N. H. Babu, and D. A. Cardwell, Phys. Rev. B **84**, 104513 (2011).

[12] M. Dean, J. Magn. Magn. Mater. **376**, 3 (2015).

[13] D. Scalapino, Phys. Rep. **250**, 329 (1995).

[14] G. L. Squires, *Introduction to the Theory of Neutron Scattering* (Cambridge University Press, Cambridge, 1978).

[15] R. Coldea, S. M. Hayden, G. Aeppli, T. G. Perring, C. D. Frost, T. E. Mason, S.-W. Cheong, and Z. Fisk, Phys. Rev. Lett. **86**, 5377 (2001).

[16] N. S. Headings, S. M. Hayden, R. Coldea, and T. G. Perring, Phys. Rev. Lett. **105**, 247001 (2010).

[17] L. J. P. Ament, G. Ghiringhelli, M. M. Sala, L. Braicovich, and J. van den Brink, Phys. Rev. Lett. **103**, 117003 (2009).

[18] L. J. Ament, M. Van Veenendaal, T. P. Devereaux, J. P. Hill, and J. Van Den Brink, Rev. Mod. Phys. **83**, 705 (2011).

[19] L. Braicovich, J. van den Brink, V. Bisogni, M. M. Sala, L. J. P. Ament, N. B. Brookes, G. M. De Luca, M. Salluzzo, T. Schmitt, V. N. Strocov, and G. Ghiringhelli, Phys. Rev. Lett. **104**, 077002 (2010).

[20] M. P. M. Dean, R. S. Springell, C. Monney, K. J. Zhou, J. Pereiro, I. Božović, B. Dalla Piazza, H. M. Rønnow, E. Morenzoni, J. van den Brink, T. Schmitt, and J. P. Hill, Nature Mater. **11**, 850 (2012).

[21] M. P. M. Dean, G. Dellea, R. S. Springell, F. Yakhou-Harris, K. Kummer, N. B. Brookes, X. Liu, Y.-J. Sun, J. Strle, T. Schmitt, L. Braicovich, G. Ghiringhelli, I. Božović, and J. P. Hill, Nature Mater. **12**, 1019 (2013).

[22] M. P. M. Dean, A. J. A. James, R. S. Springell, X. Liu, C. Monney, K. J. Zhou, R. M. Konik, J. S. Wen, Z. J. Xu, G. D. Gu, V. N. Strocov, T. Schmitt, and J. P. Hill, Phys. Rev. Lett. **110**, 147001 (2013).

[23] M. Guarise, B. D. Piazza, H. Berger, E. Giannini, T. Schmitt, H. M. Rønnow, G. A. Sawatzky, J. van den Brink, D. Altenfeld, I. Eremin, and M. Grioni, Nature Commun. **5**, 5760 (2014).

[24] S. Wakimoto, K. Ishii, H. Kimura, M. Fujita, G. Dellea, K. Kummer, L. Braicovich, G. Ghiringhelli, L. M. Debeer-Schmitt, and G. E. Granroth, Phys. Rev. B **91**, 184513 (2015).

[25] D. Meyers, H. Miao, A. C. Walters, V. Bisogni, R. S. Springell, M. d'Astuto, M. Dantz, J. Pelliciari, H. Y. Huang, J. Okamoto, D. J. Huang, J. P. Hill, X. He, I. Božović, T. Schmitt, and M. P. M. Dean, Phys. Rev. B **95**, 075139 (2017).

[26] M. Minola, G. Dellea, H. Gretarsson, Y. Y. Peng, Y. Lu, J. Porras, T. Loew, F. Yakhou, N. B. Brookes, Y. B. Huang, J. Pelliciari, T. Schmitt, G. Ghiringhelli, B. Keimer, L. Braicovich, and M. Le Tacon, Phys. Rev. Lett. **114**, 217003 (2015).

[27] M. Minola, Y. Lu, Y. Peng, G. Dellea, H. Gretarsson, M. Haverkort, Y. Ding, X. Sun, X. Zhou, D. Peets *et al.*, Phys. Rev. Lett. **119**, 097001 (2017).

[28] R. Fumagalli, L. Braicovich, M. Minola, Y. Y. Peng, K. Kummer, D. Betto, M. Rossi, E. Lefrançois, C. Morawe, M. Salluzzo, H. Suzuki, F. Yakhou, M. Le Tacon, B. Keimer, N. B.

Brookes, M. M. Sala, and G. Ghiringhelli, Phys. Rev. B **99**, 134517 (2019).

[29] Y. Peng, G. Dellea, M. Minola, M. Conni, A. Amorese, D. Di Castro, G. De Luca, K. Kummer, M. Salluzzo, X. Sun *et al.*, Nat. Phys. **13**, 1201 (2017).

[30] G. Fabbris, D. Meyers, L. Xu, V. Katukuri, L. Hozoi, X. Liu, Z.-Y. Chen, J. Okamoto, T. Schmitt, A. Uldry *et al.*, Phys. Rev. Lett. **118**, 156402 (2017).

[31] J. Kim, D. Casa, M. Upton, T. Gog, Y.-J. Kim, J. Mitchell, M. Van Veenendaal, M. Daghofer, J. van Den Brink, G. Khaliullin *et al.*, Phys. Rev. Lett. **108**, 177003 (2012).

[32] M. W. Haverkort, Phys. Rev. Lett. **105**, 167404 (2010).

[33] Y. Lu and M. W. Haverkort, Phys. Rev. Lett. **119**, 256401 (2017).

[34] C. Jia, K. Wohlfeld, Y. Wang, B. Moritz, and T. P. Devereaux, Phys. Rev. X **6**, 021020 (2016).

[35] M. Le Tacon, G. Ghiringhelli, J. Chaloupka, M. M. Sala, V. Hinkov, M. Haverkort, M. Minola, M. Bakr, K. Zhou, S. Blanco-Canosa *et al.*, Nature Phys. **7**, 725 (2011).

[36] L. Braicovich, M. M. Sala, L. Ament, V. Bisogni, M. Minola, G. Balestrino, D. Di Castro, G. De Luca, M. Salluzzo, G. Ghiringhelli *et al.*, Phys. Rev. B **81**, 174533 (2010).

[37] Y. Lu, D. Betto, K. Fürsich, H. Suzuki, H.-H. Kim, G. Cristiani, G. Logvenov, N. Brookes, E. Benckiser, M. Haverkort *et al.*, Phys. Rev. X **8**, 031014 (2018).

[38] H. Robarts, M. Barthélemy, K. Kummer, M. García-Fernández, J. Li, A. Nag, A. Walters, K. Zhou, and S. Hayden, Phys. Rev. B **100**, 214510 (2019).

[39] M. Haverkort, M. Zwierzycki, and O. Andersen, Phys. Rev. B **85**, 165113 (2012).

[40] M. W. Haverkort, in *Journal of Physics: Conference Series*, Vol. 712 (IOP Publishing, Karlsruhe, Germany, 2016), p. 012001.

[41] https://www.diamond.ac.uk/Instruments/Magnetic-Materials/I21.html.

[42] M. Kang, J. Pelliciari, Y. Krockenberger, J. Li, D. McNally, E. Paris, R. Liang, W. Hardy, D. Bonn, H. Yamamoto *et al.*, Phys. Rev. B **99**, 045105 (2019).

[43] G. Ghiringhelli, N. B. Brookes, E. Annese, H. Berger, C. Dallera, M. Grioni, L. Perfetti, A. Tagliaferri, and L. Braicovich, Phys. Rev. Lett. **92**, 117406 (2004).

[44] M. M. Sala, V. Bisogni, C. Aruta, G. Balestrino, H. Berger, N. B. Brookes, G. M. de Luca, D. D. Castro, M. Grioni, M. Guarise, P. G. Medaglia, F. M. Granozio, M. Minola, P.

Perna, M. Radovic, M. Salluzzo, T. Schmitt, K. J. Zhou, L. Braicovich, and G. Ghiringhelli, New J. Phys. **13**, 043026 (2011).

[45] F. De Groot, P. Kuiper, and G. Sawatzky, Phys. Rev. B **57**, 14584 (1998).

[46] J. Lee, B. Moritz, W. Lee, M. Yi, C. Jia, A. Sorini, K. Kudo, Y. Koike, K. Zhou, C. Monney *et al.*, Phys. Rev. B **89**, 041104 (2014).

[47] T. Devereaux, A. Shvaika, K. Wu, K. Wohlfeld, C. Jia, Y. Wang, B. Moritz, L. Chaix, W.-S. Lee, Z.-X. Shen *et al.*, Phys. Rev. X **6**, 041019 (2016).

[48] V. Bisogni, M. Moretti Sala, A. Bendounan, N. B. Brookes, G. Ghiringhelli, and L. Braicovich, Phys. Rev. B **85**, 214528 (2012).

[49] L. Chaix, E. Huang, S. Gerber, X. Lu, C. Jia, Y. Huang, D. McNally, Y. Wang, F. Vernay, A. Keren *et al.*, Phys. Rev. B **97**, 155144 (2018).

[50] C. Monney, T. Schmitt, C. E. Matt, J. Mesot, V. N. Strocov, O. J. Lipscombe, S. M. Hayden, and J. Chang, Phys. Rev. B **93**, 075103 (2016).

[51] Y. Y. Peng, E. W. Huang, R. Fumagalli, M. Minola, Y. Wang, X. Sun, Y. Ding, K. Kummer, X. J. Zhou, N. B. Brookes, B. Moritz, L. Braicovich, T. P. Devereaux, and G. Ghiringhelli, Phys. Rev. B **98**, 144507 (2018).

[52] D. Betto, R. Fumagalli, L. Martinelli, M. Rossi, R. Piombo, K. Yoshimi, D. Di Castro, E. Di Gennaro, A. Sambri, D. Bonn *et al.*, Phys. Rev. B **103**, L140409 (2021).

[53] L. J. Ament and J. v. d. Brink, arXiv:1002.3773.

[54] R. Comin, R. Sutarto, E. H. da Silva Neto, L. Chauviere, R. Liang, W. N. Hardy, D. A. Bonn, F. He, G. A. Sawatzky, and A. Damascelli, Science **347**, 1335 (2015).

[55] R. Comin, R. Sutarto, F. He, E. H. da Silva Neto, L. Chauviere, A. Fraño, R. Liang, W. N. Hardy, D. A. Bonn, Y. Yoshida, H. Eisaki, A. J. Achkar, D. G. Hawthorn, B. Keimer, G. A. Sawatzky, and A. Damascelli, Nat. Mater. **14**, 796 (2015).

[56] A. J. Achkar, F. He, R. Sutarto, C. McMahon, M. Zwiebler, M. Hücker, G. D. Gu, R. Liang, D. A. Bonn, W. N. Hardy, J. Geck, and D. G. Hawthorn, Nature Mater. **15**, 616 (2016).

[57] H. Eskes, L. Tjeng, and G. Sawatzky, Phys. Rev. B **41**, 288 (1990).

[58] M. Haverkort, Ph.D. thesis, Universität zu Köln, 2005, arXiv:cond-mat/0505214v1.